
Surflo: Consistent 3D Surface Flow Model with Global State

Antoine Guédon^{1,*} Shu Nakamura^{2,*} Nicolas Dufour^{3,*} Jiahui Lei⁴
Ko Nishino² Angjoo Kanazawa⁴

*Equal contribution.

¹LIX, École polytechnique ²Kyoto University ³Kyutai ⁴UC Berkeley

antoine.guedon@enpc.fr

<https://anttwo.github.io/surflo>



Figure 1: **Surflo turns a handful of unposed RGB views into a detailed 3D surface.** From a variable number of input views (*left*), Surflo encodes the scene into a fixed-size latent and decodes it via flow matching into an arbitrary number of oriented surface points, yielding a clean mesh (*middle*). Per-view feed-forward models [68, 45] instead emit overlapping pointmaps (*right*) that complicate mesh extraction. Surflo exceeds them in quality, while running an order of magnitude faster than state-of-the-art optimization-based methods like Gaussian Wrapping [20], which require hundreds of views. All results are from the same 16 unposed input images, a sparse set of screenshots from an in-the-wild video of the *Gallos* sculpture at Tintagel Castle, UK.

Abstract

Geometry is invariant to viewpoint, which makes any collection of images a redundant encoding of a single 3D state. Existing feed-forward reconstruction models fail to exploit this: per-view methods emit overlapping, unaligned pointmaps that grow linearly with input count, while global-latent methods commit to a fixed, low-resolution output. We introduce Surflo, which compresses a variable number of unposed RGB views into K latent tokens—one global state—and decodes oriented 3D surface points by independently transporting them from noise onto the surface via flow matching. This frees the output from any fixed grid or token budget: the same latent yields from a few thousand to a million points in a single forward pass. To suppress the local inconsistencies inherent to independent per-point decoding, an inference-time guidance term correlates nearby points by injecting a photometric gradient during ODE integration. Surflo matches or surpasses feed-forward baselines on surface metrics, runs an order of magnitude faster than optimization-based methods that require hundreds of views, and is the only feed-forward approach to combine a global latent with arbitrary-resolution decoding.

1 Introduction

In the spirit of Klein’s Erlangen program [41], 3D geometry is precisely what remains invariant under the viewing transformation. It follows that a collection of images of a scene is a redundant encoding of its geometry: the same underlying 3D state is re-projected into every view, modulo the camera. As more views are gathered, the raw pixel data grows linearly while the geometric content does not—additional views serve only to resolve ambiguities and refine a shared, global state. For downstream applications such as real2sim for robotics [4] and agent navigation [79], it is this global geometry that is the target; the images are merely the instruments used to recover it.

This observation has a direct architectural consequence: if many views encode one geometry, the right intermediate representation is a single global state, not a per-view or per-pixel one. We present **Surflo**, a feed-forward model built around this principle. Given a variable number of unposed RGB views, Surflo compresses them into a single compact and consistent global representation of the 3D scene. Rather than being bound to a fixed spatial grid or a rigid token budget, the underlying geometry can be queried from this global state by sampling an arbitrary number of oriented surface points—from a few thousand to a million per scene. The resulting output is global, consistent across views, and readily converted into a mesh.

Existing feed-forward methods fall short of this principle along two distinct axes. *Per-view* models such as VGGT [68, 73, 45] predict a separate pointmap per input image, preserving the very view-wise redundancy a global representation should compress away: their token count grows linearly with views, and the pointmaps overlap heavily without exact alignment, resisting fusion into a clean mesh (Figure 1). The few methods that summarize the scene in a single latent pay a different price: Chen et al. [11] compresses few-view inputs into a fixed-size code but reads it out as a small, fixed set of $10K$ points, and Wang et al. [70] maintains a persistent state decoded as per-view RGB rather than a global geometric object. D4RT [91] also adopts a scene representation queried for independent points, but operates on dense videos and regresses positions of *pixel-anchored* queries rather than generatively sampling free oriented surface points from sparse views as Surflo does.

Building a representation that is both globally compressed and geometrically queryable requires three coupled ingredients: (1) compression of an unbounded number of multi-view tokens into a fixed-size representation without loss of scene-specific detail, (2) decoding of that global representation into an arbitrary number of surface points, and (3) consistency across the decoded geometry. First, the encoder of Surflo builds on a frozen VGGT [68] backbone for its strong geometric features: patch tokens from several intermediate layers are enriched with a 3D positional encoding of their unprojected position and compressed into K latent tokens. The decoder then generates oriented surface points via flow matching [47], but unlike standard generation on fixed grids it denoises each point independently: conditioned on the global latent, it predicts a velocity that transports an individual query point from a source distribution onto the surface. The same independence, however, has a cost—nothing forces independently sampled points to land on the same surface, so ambiguity in occluded regions can produce local inconsistencies. We resolve this with a guidance mechanism, reminiscent of loss-conditioned diffusion guidance [5], that correlates nearby points at inference time: injecting the gradient of a photometric and depth loss into the predicted velocity aligns the output with the visible images and suppresses noisy outliers.

Across 8 3D reconstruction benchmarks, Surflo matches or surpasses recent feed-forward baselines on surface metrics while being the only feed-forward method that decodes geometry at arbitrary resolution from a single shared latent. The contributions of this work can be summarized as follows:

- A feed-forward encoder, built on a frozen VGGT backbone [68], that compresses a variable number of unposed RGB views into a single global state independent of view count.
- A flow-matching decoder that reads out this latent as an oriented surface by transporting oriented points in $\mathbb{R}^3 \times \mathbb{S}^2$ independently, enabling arbitrary output resolution from the same shared latent.
- A rendering-based guidance scheme during ODE integration that correlates nearby points and aligns the decoded surface with the input images, mitigating the outliers typical of independent per-point decoding.
- As an auxiliary contribution, a meshed version of the DL3DV [46] dataset: each of the $\sim 10.5K$ scenes is enriched with a watertight surface mesh and $\sim 10^7$ oriented points obtained via Gaussian Wrapping [20]. To our knowledge, this is the first real scene-level watertight mesh dataset at this scale, and we will release the data as well as the code upon publication.

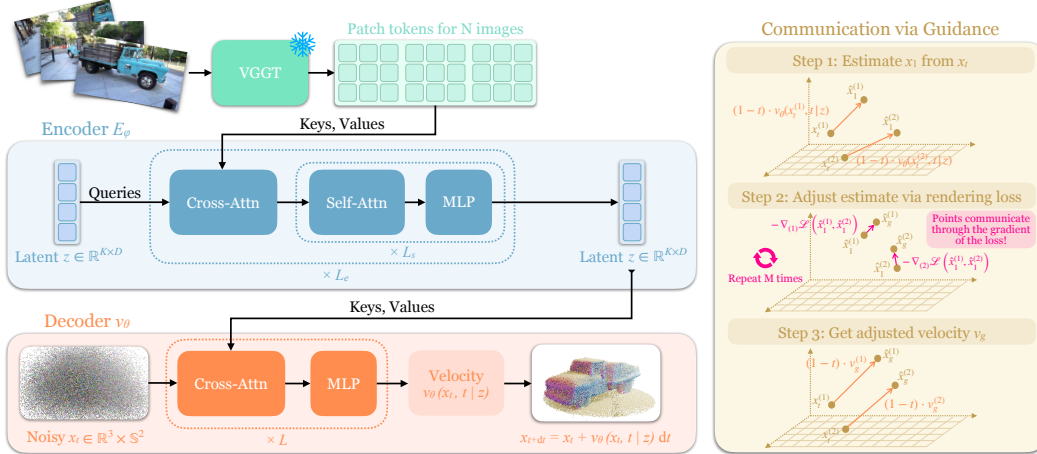


Figure 2: **Three key ingredients define Surflo.** **Encoder:** a frozen VGGT [68] maps N unposed RGB views to patch tokens, which a Perceiver-style compressor with K learnable queries distills into a fixed-size latent $\mathbf{z} \in \mathbb{R}^{K \times D}$. **Decoder:** each query $\mathbf{x}_t \in \mathbb{R}^3 \times \mathbb{S}^2$ is diffused *independently* via cross-attention with \mathbf{z} to a velocity v_θ ; any number of points can be integrated in parallel. **Guidance** (Sec. 2.3): for $t \geq 0.95$, at each step of the ODE integration, per-point velocities are coupled [5] via M gradient steps on a global rendering loss \mathcal{L} .

2 Method

Our goal is to recover scene geometry from a variable number of input images at a variable output resolution, with both chosen freely at inference. The design of Surflo follows directly from this goal. To support an arbitrary number of input views N , the conditioning representation must have a size independent of N . Recent multi-view foundation models [68, 74, 45] integrate observations across views and produce geometry-aware features, but their token count grows linearly with N . We therefore compress these features into a *fixed-size* latent \mathbf{z} . To support an arbitrary number of output points P , we decode each query point *independently*: a per-point estimator maps each query $\mathbf{x} \in \mathbb{R}^3 \times \mathbb{S}^2$ to a surface sample (3D coordinates and normal). Decoding P points thus reduces to P independent, batched forward passes. To ensure that independently sampled queries fall onto a coherent surface, we introduce an inference-time guidance term that correlates nearby points. Putting these together, Surflo operates as follows (Figure 2):

1. An *encoder* E_ϕ that maps $\{\mathbf{I}_n\}_{n=1}^N$ to a fixed-size latent $\mathbf{z} \in \mathbb{R}^{K \times D}$, independent of N .
2. A *flow-matching decoder* v_θ that, given \mathbf{z} , a time $t \in [0, 1]$, and a query $\mathbf{x}_t \in \mathbb{R}^3 \times \mathbb{S}^2$, predicts a velocity transporting \mathbf{x}_t toward the scene surface $\mathcal{S} \subset \mathbb{R}^3$ and its normals.
3. A *guided ODE solver* that, at inference, integrates v_θ together with a rendering-based coupling term to produce a coherent surface.

2.1 Encoder: From Images to a Fixed-size Global State

Frozen VGGT backbone. We rely on a frozen foundation model, namely VGGT [68], as the backbone for its strong geometry-aware features. For each input view \mathbf{I}_n , VGGT produces a stack of patch tokens together with a single camera token. Following the procedure of Wang et al. [68], we extract and concatenate patch tokens from four layers $\ell \in \{4, 11, 17, 23\}$, then project them to a working dimension D . This yields a per-view set of tokens $\mathbf{T}_n \in \mathbb{R}^{4N_p \times D}$, where N_p is the number of patches per image. We apply a similar projection to the per-view camera tokens $\mathbf{C}_n \in \mathbb{R}^{4 \times D}$.

3D positional encoding. We augment each patch token with a 3D positional encoding. We read off the 3D coordinates of the patch centers in the corresponding VGGT pointmaps, yielding $\mathbf{p}_n \in \mathbb{R}^{N_p \times 3}$; we then map them to Fourier features $\gamma(\mathbf{p}_n) \in \mathbb{R}^{N_p \times D}$ [64], and add the result to the patch tokens. A similar encoding γ is reused by the decoder for query points. This shared encoding is the only mechanism that gives the decoder a notion of *where* in 3D space a query lies relative to the encoded scene. Without it, the latent \mathbf{z} stores observations from VGGT’s view-aggregated coordinate frame, while decoder queries arrive as raw coordinates with no a priori relationship to that frame; the



Figure 3: **Surflo denoises 3D points into an oriented surface.** From a variable number of input views (a), Surflo denoises an arbitrary number of noisy 3D points and normals (b) into an oriented surface (c). Integrating the flow-matching velocity without guidance already achieves high accuracy but can exhibit outliers and miss fine details. We therefore introduce two guidance terms. A photometric guidance term $\nabla_{\mathbf{x}} \mathcal{L}_{\text{photo}}$ computed by instantiating Gaussian Splatting [40] on the points, pulls them onto surfaces consistent with the input views and recovers finer details (d). An optional monocular depth [45] guidance further sharpens geometry (e).

alignment would have to be learned implicitly, across whatever coordinate system VGGT produces for each scene. With shared γ , a query point near a VGGT patch shares similar Fourier features with it, so cross-attention localizes relevant scene information by spatial proximity rather than learned association—making coordinate-frame robustness structural rather than something the decoder must absorb during training.

Compression. We compress the union of $N \times 4N_p$ position-encoded patch tokens $\{\mathbf{T}_n + \gamma(\mathbf{p}_n)\}_{n=1}^N$ with a Perceiver-style cross-attention module [33, 34]. A fixed set of $K (\ll N \times 4N_p)$ learned latent queries $\mathbf{z}_p^{(0)} \in \mathbb{R}^{K \times D}$ cross-attends to the patch tokens, followed by L_s self-attention blocks:

$$\mathbf{z}_p^{(l+1)} = \text{SelfAttn}^{L_s}(\text{CrossAttn}(\mathbf{z}_p^{(l)}, \{\mathbf{T}_n + \gamma(\mathbf{p}_n)\}_n)) \in \mathbb{R}^{K \times D}. \quad (1)$$

This process is iterated L_e times to obtain the final latent $\mathbf{z}_p := \mathbf{z}_p^{(L_e)}$. Camera tokens $\{\mathbf{C}_n\}_n$ are processed by a similar but lighter Perceiver into a single latent $\mathbf{z}_c \in \mathbb{R}^{1 \times D}$ encoding additional information about the current world space of the scene, and concatenated into $\mathbf{z} := [\mathbf{z}_p, \mathbf{z}_c]$.

2.2 Flow-Matching Decoder with Independent Query Points

Per-point flow. We treat surface decoding as transporting individual query points in $\mathbb{R}^3 \times \mathbb{S}^2$ from a source distribution p_0 to the surface distribution p_1 , conditioned on the latent representation \mathbf{z} . We adopt the flow-matching formulation of Lipman et al. [47]: at training time, we sample a target $\mathbf{x}_1 \sim p_1$, a source $\mathbf{x}_0 \sim p_0$, a time $t \sim \text{LogitNormal}(1, 1.6)$, and form the linear interpolant $\mathbf{x}_t = (1-t)\mathbf{x}_0 + t\mathbf{x}_1$ with conditional velocity $u(\mathbf{x}_t, t) = \mathbf{x}_1 - \mathbf{x}_0$.

Decoder architecture. The decoder v_θ is an L -layered transformer that ingests a Fourier-encoded query point $\gamma(\mathbf{x}_t)$ and predicts a velocity through cross-attention to the latent \mathbf{z}_p and an MLP. The prediction of the velocity is also conditioned on the time and camera token $[\tau(t), \mathbf{z}_c]$ through Ada-LN [56] blocks before each cross-attention and MLP, where τ is a sinusoidal time embedding, allowing the decoder to adjust its prediction to the current time and world space of the scene.

Training objective. The training objective is the standard flow-matching loss

$$\mathcal{L}_{\text{FM}}(\theta, \phi) = \mathbb{E}_{t, \mathbf{x}_0, \mathbf{x}_1, \{\mathbf{I}_n\}_n} \|v_\theta(\mathbf{x}_t, t | \mathbf{z}) - (\mathbf{x}_1 - \mathbf{x}_0)\|_2^2. \quad (2)$$

The loss decomposes over independent query points, allowing us to train on thousands of points per scene while keeping a single shared latent in memory. Parameters θ and ϕ are learnt jointly, as the decoder and encoder are trained together in an end-to-end fashion.

Source distribution. Each query’s normal is initialized uniformly on \mathbb{S}^2 . Initializing the 3D coordinate from $\mathcal{N}(0, \mathbf{I}_3)$, however, wastes model capacity on empty space and slows convergence. We instead sample from a mixture of Gaussians centered on perturbed VGGT pointmap samples, with noise σ_s large enough to cover surfaces occluded in the input views (Figure 3). This concentrates the flow near the geometry while leaving room to fill in occluded regions.

Inference. At inference, we sample P query points $\{\mathbf{x}_0^{(m)}\}_{m=1}^P$ from p_0 and integrate $\frac{d\mathbf{x}_t}{dt} = v_\theta(\mathbf{x}, t, \mathbf{z})$ from $t=0$ to $t=1$ with a simple Euler solver. Because all P queries share the same latent \mathbf{z} , the per-point cost is dominated by the relatively small decoder, and we can decode $P = 10^3$ to $P = 10^6$ points in a batched pass on a single GPU. As a result, depending on the requested number of samples, the same scene latent supports both a fast coarse preview and a dense surface (Figure 5).

2.3 Communication via Guidance

Per-point independence gives Surflo its flexibility, but at a cost: Equation (2) models each query in isolation, never the joint distribution over surface points. As a result, independently sampled queries are not constrained to land on the same physical surface, producing scattered points between surfaces and drift from the input views. We therefore augment the deterministic flow with a *communication-via-guidance* term, in the spirit of universal guidance [5, 26], injecting the gradient of a differentiable-rendering [40, 88, 24] loss into each ODE step so independently sampled queries can coordinate through a shared global signal.

Specifically, near the end of the ODE integration, for $t \geq 0.95$, we predict at each ODE step the corresponding target points $\hat{\mathbf{x}}_1 = \mathbf{x}_t + (1-t)v_\theta$ and run M gradient-descent steps on a global communication loss $\mathcal{L}_{\text{render}}$ that depends on the entire batch. This process couples all points and adjusts the estimated target points, yielding a guided target $\hat{\mathbf{x}}_1^g$ and the corresponding guided velocity $v_g = (\hat{\mathbf{x}}_1^g - \mathbf{x}_t)/(1-t)$ used for the actual Euler step $\mathbf{x}_{t+dt} = \mathbf{x}_t + dt v_g$.

In practice, we use a rendering-based loss: we treat the set of predicted targets $\hat{\mathbf{x}}_1$ as a cloud of small oriented Gaussians and *render* them through the cameras recovered by the pretrained VGGT backbone to obtain images $\hat{\mathbf{I}}_n(t)$ at the input view poses. Following Gaussian Wrapping [20], we then compute a rendering loss against the input views:

$$\mathcal{L}_{\text{render}}(\{\hat{\mathbf{x}}_1\}) = \frac{1}{N} \sum_{n=1}^N \lambda \|\hat{\mathbf{I}}_n(t) - \mathbf{I}_n\|_1 + (1-\lambda) \text{DSSIM}(\hat{\mathbf{I}}_n(t), \mathbf{I}_n), \quad (3)$$

including additional regularization terms on rendered depth maps [20, 24].

The updated velocities *couple* the query points: nearby queries that disagree about a surface receive a shared corrective signal, which acts as a soft consistency prior. The rendering objective also encourages the points to match the input images and improves the quality of the details considerably. Optionally, we strengthen guidance with a monocular-depth expert [45] (Figure 3). Monocular depth predictions are not multi-view consistent, but their relative ordering provides a strong guidance signal via depth-order regularization [24, 23].

The resulting oriented Gaussians are converted into a triangle mesh via Delaunay triangulation, following [20].

2.4 Training data: Explicit Surfaces for DL3DV

Scene-level 3D surface datasets of real environments do not exist at the scale we need: Tanks & Temples [42] or BlendedMVS [84] contain only a few dozen scenes, and DL3DV [46] provides multi-view images and COLMAP poses but no surface ground truth. As an auxiliary contribution, we close this gap by enriching each of the $\sim 10.5\text{K}$ DL3DV scenes with a watertight mesh and an oriented point cloud. For each scene, we run Gaussian Wrapping [20] on the full set of views to extract a watertight surface, and sample 10^7 points and normals from the mesh, discarding outliers via a visibility check against the input views. We will release this dataset and expect it to be useful for scene-level surface learning beyond Surflo.

We use this dataset as our ground-truth surface distributions p_1 . At each training step, we first sample 12 scenes; then, we draw $N \in [2, 16]$ input views for each scene as well as a batch of $\sim 8\text{K}$ points uniformly on each ground-truth surface; finally, we run our model, align the ground-truth points with our predicted points, and minimize equation (2). More details can be found in Appendix. Rendering guidance is only applied at inference; the encoder backbone (VGGT) is kept frozen throughout.

3 Experiments

We evaluate Surflo on several few-view 3D reconstruction benchmarks, against representative per-view, latent and optimization-based baselines, and ablate its main design choices. As shown in Figure 4, Surflo remains robust even in challenging capture conditions, including scenes with strong exposure variation across views and transparent objects, such as the semi-transparent figure in the last row.

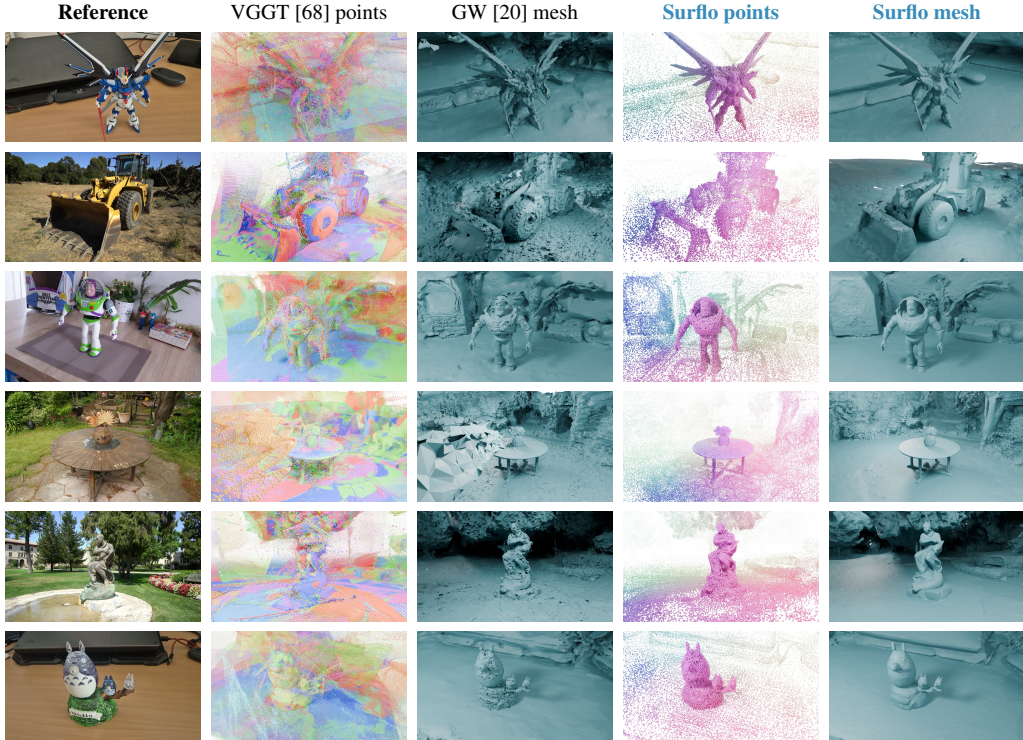


Figure 4: **Qualitative comparisons from 16 unposed input views.** From left to right: reference view, VGGT [68] pointmaps (one color per view), Gaussian Wrapping [20] mesh from VGGT initialization, and Surflo’s points and mesh. VGGT pointmaps are noisy and duplicated across views, and per-scene GW struggles from few inputs; Surflo yields well-distributed surface points and a clean mesh from the same shared latent.

3.1 Setup

Datasets. We train on the $\sim 10.5\text{K}$ scenes of DL3DV [46] with ground-truth surfaces obtained from Gaussian Wrapping [20], and split out a held-out test set. We evaluate on two groups of out-of-distribution benchmarks. The first group ships with native surface ground truth: ML-Hypersim [58], BlendedMVS [84], DTU [1], and SCRREAM [36]. For the second group, no whole-scene surface ground truth is available, and we generate pseudo-ground-truth surfaces from the dense view sets using the same Gaussian Wrapping pipeline we apply at training time. This group includes our DL3DV test split, Mip-NeRF 360 [6] and DeepBlending [27]. We also include Tanks & Temples [42]: its native ground truth covers only the foreground object of each scene, and our pseudo-GT additionally captures the background geometry. This second evaluation lets us quantify the geometry gap between feed-forward models that observe only a few input views and the best surfaces that can be extracted from a dense RGB capture. For evaluation, each test scene is reconstructed from a fixed set of 16 unposed input views unless stated otherwise.

Metrics. We report Chamfer Distance (CD_\downarrow) between predicted and ground-truth point clouds (normalized by the spatial extent of the scene) and F1-score (F1_\uparrow) at a fixed scene-relative threshold of 1% of the scene diagonal, following standard practice.

Baselines. We compare Surflo against three families of baselines for scene-level surface reconstruction, all of which receive the same input views (from 2 to 16 views) unless stated otherwise. (i) *Per-view feed-forward*: the raw pointmaps of VGGT [68] and DepthAnything-3 [45], together with their TSDF-fused [15] variants for turning per-view predictions into a single mesh. Because pointmap outputs do not represent a single coherent surface, they trade physical consistency for purely local accuracy; we therefore report them *for reference only* and exclude them from the ranking. (ii) *Latent feed-forward*: NOVA3R [11], which compresses the input views into a latent but reads it out as a fixed-size point cloud. NOVA3R is evaluated with randomly sampled 2 views every time, as it is trained with 2 input views only and feeding more than 2 views systematically results in

Table 1: **Quantitative Evaluation** on four datasets where reference surfaces are generated from Gaussian Wrapping [20] on dense views, covering both foreground and background. DL3DV [46] corresponds to our held-out test split (in-distribution), Tanks & Temples [42], Mip-NeRF 360 [6] and DeepBlending [27] are out-of-distribution benchmarks. All methods are evaluated from the same set of 16 unposed input views per scene. Per-view feed-forward baselines come in two flavours: (i) the raw *pointmap* variants (greyed), which simply concatenate per-view depth predictions into a multi-layered point set without enforcing inter-view consistency, and (ii) their TSDF [15]-fused counterparts, which collapse the per-view depths into a single global mesh.

Method	DL3DV		Tanks&Temples		Mip-NeRF 360		DeepBlending	
	CD↓	F1↑	CD↓	F1↑	CD↓	F1↑	CD↓	F1↑
<i>Per-view feed-forward (no global surface)</i>								
VGGT pointmap [68]	0.0100	74.84	0.0076	81.04	0.0132	69.18	0.0110	76.89
DA3 pointmap [45]	0.0097	77.42	0.0156	71.96	0.0144	67.59	0.0132	67.84
<i>Per-view feed-forward (fused global surface)</i>								
VGGT + TSDF [68]	0.0126	69.23	0.0113	77.46	0.0178	60.64	0.0193	62.30
DA3 + TSDF [45]	0.0120	72.30	0.0177	70.80	0.0182	59.91	0.0210	54.03
<i>Latent feed-forward (fixed-size output)</i>								
NOVA3R [11]	0.0459	30.51	0.0432	32.99	0.0429	25.60	0.0550	27.61
<i>Per-scene optimization (sparse-view)</i>								
2DGS [31]	0.0163	60.10	0.0161	62.95	0.0222	51.08	0.0204	59.54
RaDe-GS [88]	0.0166	59.48	0.0170	61.67	0.0224	50.83	0.0202	60.04
Gaussian Wrapping [20]	0.0168	60.67	0.0157	64.94	0.0201	57.86	0.0164	64.54
Surflo (ours) - No guidance	0.0072	81.92	0.0053	88.57	0.0068	82.00	0.0116	70.96
Surflo (ours) - With guidance	0.0083	78.55	0.0056	86.40	0.0103	76.57	0.0109	75.09

blurry reconstructions. We restrict our comparisons to methods targeting scene-level reconstruction and therefore exclude object-centric feed-forward models such as ReconViaGen [9]: their outputs cover only foreground objects and would yield uninformative scene-level metrics, as most of the surrounding geometry would be missing. (iii) *Per-scene optimization*: 2DGS [31], RaDe-GS [88], and Gaussian Wrapping [20] run on the same sparse views with camera parameters and initial points estimated by VGGT. These baselines highlight how strongly per-scene optimization underperforms in the few-view regime, and motivate the use of a learned prior.

Implementation details. The encoder uses a frozen VGGT-1B backbone, a Perceiver compressor with $K = 128$ latent tokens of dimension $D = 512$, $L_s = 4$ self-attention blocks per cross attention, and Gaussian Fourier features [64] with $F = 512$ frequencies. The decoder is a 12-layer transformer that cross-attends to the latent for the first 6 layers. We train with AdamW, batch size 12 scenes, 8K query points per scene per step, on $4 \times \text{H100}$ GPUs for 400K iterations. At inference, we use an Euler ODE solver with 150 steps, and decode 100K points by default, though this number can be adjusted at will; Figure 5 illustrates reconstructions with different numbers of points. Optionally, we apply photometric guidance starting from $t = 0.95$, and perform $M = 32$ loss updates at each ODE step.

3.2 Results

Main Results. Table 2 reports surface metrics on the four out-of-distribution benchmarks with native surface ground truth, and Table 1 reports the same metrics on DL3DV, T&T, Mip-NeRF 360 and DeepBlending, where reference surfaces are generated by Gaussian Wrapping on the dense view sets. All methods receive the same 16 input views. The two tables tell a consistent story: per-view baselines, while accurate per-frame, accumulate misalignments when their pointmaps are merged, and their fused meshes show duplicated surfaces and eroded or floating geometry, particularly at view boundaries. NOVA3R [11] produces coarse and eroded outputs as its decoder is forced to a fixed point budget. Surflo outperforms the best optimization-based references in absolute Chamfer at a fraction of the cost (see Efficiency in Section 3.2), and is the only feed-forward model that also supports decoding the same latent at any chosen resolution. Figure 4 shows qualitative comparisons.

Varying number of input views. Beyond the 16-view protocol used on all datasets above, we further study how Surflo behaves as the number of input views changes. Because the encoder compresses any number of views into a fixed-size latent, the same model can be evaluated across capture densities without retraining or any architectural change. Tables 3 and 4 report this experiment on two out-of-distribution datasets, Tanks & Temples and Mip-NeRF 360, as the number of unposed input views per scene varies from 2 to 32. Surflo is consistently best across all view counts, including the very

Table 2: **Quantitative Evaluation** on four out-of-distribution benchmarks with native surface ground truth: ML-Hypersim [58], BlendedMVS [84], DTU [1], and SCRREAM [36]. We report Chamfer Distance (CD, ↓) and F1-score (F1, ↑). All methods are evaluated from the same set of 16 unposed input views per scene. Per-view feed-forward baselines come in two flavours: (i) the raw *pointmap* variants (greyed), which simply concatenate per-view depth predictions into a multi-layered point set without enforcing inter-view consistency, and (ii) their TSDF [15]-fused counterparts, which collapse the per-view depths into a single global mesh.

Method	ML-Hypersim		BlendedMVS		DTU		SCRREAM	
	CD↓	F1↑	CD↓	F1↑	CD↓	F1↑	CD↓	F1↑
<i>Per-view feed-forward (no global surface)</i>								
VGGT pointmap [68]	0.0070	91.91	0.0105	79.98	0.0249	47.80	0.0063	83.36
DA3 pointmap [45]	0.0071	87.16	0.0739	66.74	0.0714	26.35	0.0063	83.26
<i>Per-view feed-forward (fused global surface)</i>								
VGGT + TSDF [68]	0.0138	74.08	0.0270	59.64	0.0380	28.93	0.0226	59.89
DA3 + TSDF [45]	0.0151	69.07	0.0875	52.61	0.0801	17.93	0.0220	60.95
<i>Latent feed-forward (fixed-size output)</i>								
NOVA3R [11]	0.0635	27.65	0.0413	32.13	0.0307	31.41	0.0771	27.41
<i>Per-scene optimization (sparse-view)</i>								
2DGS [31]	0.0176	62.03	0.0295	48.19	0.0394	28.78	0.0234	53.57
RaDe-GS [88]	0.0174	62.68	0.0303	48.85	0.0393	28.30	0.0242	53.52
Gaussian Wrapping [20]	0.0145	66.86	0.0259	55.64	0.0460	30.17	0.0123	62.96
Surflo (ours) - No guidance	0.0097	77.98	0.0103	76.50	0.0242	39.23	0.0114	61.20
Surflo (ours) - With guidance	0.0079	87.97	0.0114	77.28	0.0240	42.05	0.0070	81.11

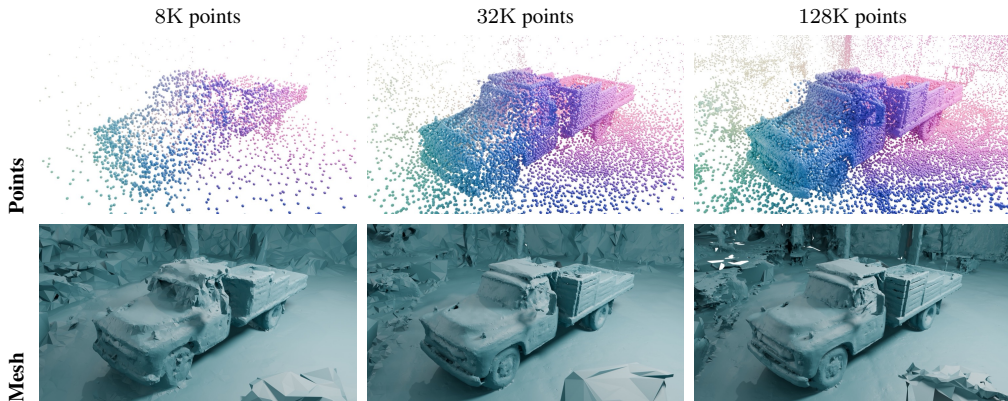


Figure 5: **Variable-resolution decoding from a single shared latent.** Left to right: the flow-matching decoder is queried more densely; *the latent is unchanged across columns*. Bottom: mesh extracted from each point set.

sparse 2-view regime. While Surflo benefits from additional views, the size of the latent does not grow with the number of views. Figure 6 shows that even from very few views the model already produces a coherent surface; additional views progressively fill previously missing geometry and sharpen fine detail, while the decoding cost remains unchanged.

Multi-resolution decoding. A key feature of Surflo is that the latent itself does not change with the requested output resolution. Figure 5 shows the same scene latent decoded at three resolutions, from 8K to 128K points, on the same GPU. The coarse output is suitable for fast collision queries or scene previews, while the dense output offers sharper details and background geometry.

Ablations. Table 5 ablates the three main design choices of Surflo. **Latent size.** Increasing K from 32 to 128 tokens consistently improves both metrics. We use $K = 128$ throughout. **Source distribution.** Replacing our noisy-VGGT-pointmap source with a pure Gaussian source degrades reconstruction, especially for large scenes. **3D positional encoding.** Augmenting VGGT tokens with our 3D positional encoding improves both metrics.

Photometric guidance. Disabling the guidance term can introduce visible noisy outliers, while still resulting in high accuracy. Full photometric guidance is consistently best for visual quality.

Efficiency. We additionally report wall-clock numbers on a single H100 GPU: encoding a 16-view scene takes a single forward pass through VGGT and the Perceiver compressor; the latent is then

Table 3: **Varying number of input views** on Tanks&Temples. We report Chamfer Distance (CD, ↓) and F1-score (F1, ↑) as the number of unposed input views per scene varies from 2 to 32. Best, second-best and third-best are highlighted; greyed per-view pointmap variants are reported for reference and excluded from the ranking.

Method	2 views		4 views		8 views		32 views	
	CD↓	F1↑	CD↓	F1↑	CD↓	F1↑	CD↓	F1↑
<i>Per-view feed-forward (no global surface)</i>								
VGGT pointmap [68]	0.1461	5.27	0.0224	65.67	0.0082	80.61	0.0064	87.44
DA3 pointmap [45]	0.1595	6.79	0.0247	54.88	0.0177	67.38	0.0128	74.63
<i>Per-view feed-forward (fused global surface)</i>								
VGGT + TSDF [68]	0.1444	6.83	0.0285	53.62	0.0138	70.85	0.0094	84.83
DA3 + TSDF [45]	0.1428	6.97	0.0293	47.90	0.0210	61.64	0.0140	74.59
<i>Latent feed-forward (fixed-size output)</i>								
NOVA3R [11]	0.2620	5.78	0.0502	30.29	0.0557	31.78	0.0423	35.54
<i>Per-scene optimization (sparse-view)</i>								
2DGS [31]	0.1453	6.09	0.0316	43.05	0.0187	55.95	0.0152	68.43
RaDe-GS [88]	0.1454	6.30	0.0314	42.60	0.0191	55.67	0.0156	66.24
Gaussian Wrapping [20]	0.1476	5.24	0.0313	45.28	0.0176	60.04	0.0133	72.10
Surflo (ours) - No guidance	0.1345	9.28	0.0135	75.07	0.0059	86.59	0.0049	90.76
Surflo (ours) - With guidance	0.1416	7.08	0.0198	72.65	0.0061	86.25	0.0049	90.34

Table 4: **Varying number of input views** on Mip-NeRF 360. We report Chamfer Distance (CD, ↓) and F1-score (F1, ↑) as the number of unposed input views per scene varies from 2 to 32. Best, second-best and third-best are highlighted; greyed per-view pointmap variants are reported for reference and excluded from the ranking.

Method	2 views		4 views		8 views		32 views	
	CD↓	F1↑	CD↓	F1↑	CD↓	F1↑	CD↓	F1↑
<i>Per-view feed-forward (no global surface)</i>								
VGGT pointmap [68]	0.0765	8.33	0.0310	47.62	0.0166	67.93	0.0133	74.90
DA3 pointmap [45]	0.0750	8.35	0.0300	45.45	0.0168	66.73	0.0139	73.72
<i>Per-view feed-forward (fused global surface)</i>								
VGGT + TSDF [68]	0.0755	9.63	0.0326	40.79	0.0244	55.29	0.0161	65.56
DA3 + TSDF [45]	0.0746	9.24	0.0322	40.31	0.0220	55.17	0.0162	64.75
<i>Latent feed-forward (fixed-size output)</i>								
NOVA3R [11]	0.0795	8.46	0.0642	21.41	0.0492	28.01	0.0562	18.95
<i>Per-scene optimization (sparse-view)</i>								
2DGS [31]	0.0754	8.73	0.0344	37.15	0.0283	47.45	0.0217	52.13
RaDe-GS [88]	0.0756	8.76	0.0352	37.11	0.0293	47.89	0.0215	53.08
Gaussian Wrapping [20]	0.0766	7.28	0.0339	41.61	0.0251	53.97	0.0162	62.41
Surflo (ours) - No guidance	0.0714	13.07	0.0192	58.68	0.0127	74.07	0.0071	81.24
Surflo (ours) - With guidance	0.0736	10.40	0.0263	53.71	0.0145	73.44	0.0137	80.66

re-used for all subsequent queries. Decoding 10^5 points from the cached latent takes a few seconds, dominated by the ODE solve, which is two orders of magnitude faster than per-scene optimization baselines such as 2DGS or Gaussian Wrapping. A small number of guidance steps adds modest overhead (typically from 30 seconds to 3 minutes depending on the number of guidance steps), as rendering Gaussians is inexpensive and independent of the number of views N .

4 Related Work

We provide a focused summary here; a comprehensive discussion is available in Appendix A.

Per-view feed-forward 3D. One class of models predicts geometry—typically depth or pointmaps—separately for each input image. DUST3R [73] and VGGT [68] produce highly accurate local geometry, but their output is *view-bound*: the number of predicted tokens grows linearly with the number of inputs. These per-view outputs are often redundant and misaligned, making them difficult to fuse into a consistent global mesh [4]. Surflo differs by producing a single, fixed-size latent that represents the entire scene regardless of the number of input views.

Global latent models. Other works seek a view-agnostic representation. CUT3R [70] maintains a persistent state but still decodes it into per-view pointmaps. NOVA3R [11] is the closest to our work, using a flow-matching head to decode points from a latent. However, NOVA3R is restricted to a fixed

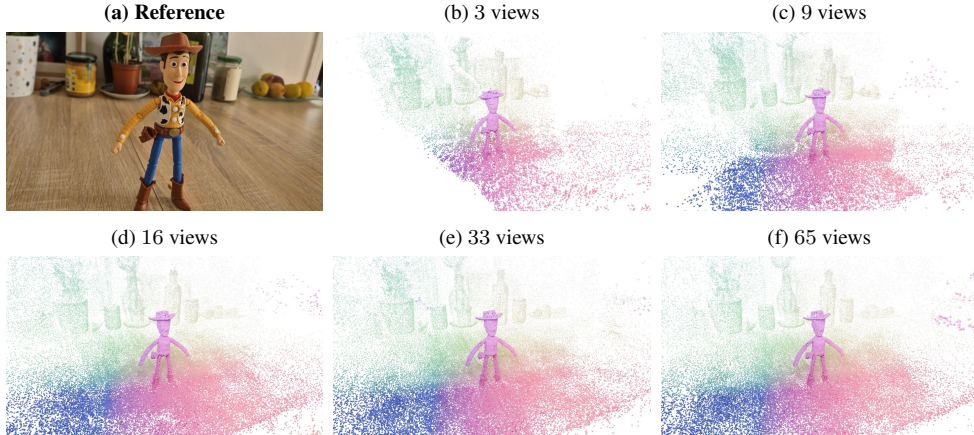


Figure 6: **Surflo reconstructions with a varying number of input views.** More views progressively complete the scene and sharpen fine detail; the decoder cost is unchanged, since all five reconstructions are produced from a single fixed-size latent. Surflo therefore handles a wide range of capture densities without retraining or architectural change.

Table 5: Ablation study on the DL3DV test split (in-distribution) and Tanks & Temples (out-of-distribution), with 16 input views. We vary one design choice at a time and report Chamfer Distance (CD \downarrow) and F1 (F1 \uparrow).

Component	Variant	DL3DV		Tanks & Temples	
		CD \downarrow	F1 \uparrow	CD \downarrow	F1 \uparrow
Latent size	$K = 32$ tokens	0.0089	72.76	0.0068	79.51
	$K = 128$ tokens	0.0073	81.21	0.0055	88.02
3D PE on VGGT tokens	None (raw VGGT tokens)	0.0083	76.05	0.0068	80.78
	Gaussian Fourier 3D PE	0.0073	81.21	0.0055	88.02
Source distribution	Pure Gaussian $\mathcal{N}(0, \sigma^2 I)$	0.0088	73.57	0.0074	77.09
	Mixture of Gaussians	0.0073	81.21	0.0055	88.02

output of 10K points and is trained on only two views, limiting its ability to reconstruct full scenes. In contrast, Surflo supports decoding an arbitrary number of oriented surface points from a global state.

Flow matching and guidance. Our decoder builds on flow matching [47, 50], which has shown success in generating point clouds and meshes for single objects [55, 80, 90]. Unlike these methods, which often operate on fixed grids or structured latents, Surflo predicts a velocity field that transports query points independently, reminiscent of MAR [44]. This independence is regularized by a guidance mechanism reminiscent of loss-conditioned diffusion [5, 61]. While previous guidance methods typically use external classifiers, our guidance signal is derived directly from a differentiable photometric loss to ensure consistency with the input images.

Per-scene optimization. High-fidelity reconstruction at the scene scale is traditionally dominated by optimization-based methods like NeuS [69] or 3D Gaussian Splatting [40]. These methods produce excellent surfaces but require hundreds of *posed* images and significant per-scene compute time. Surflo provides a feed-forward alternative: it produces a reusable scene latent in a single pass, decoupling the cost of the final reconstruction from the number of input images.

5 Conclusion

We presented Surflo, a feed-forward 3D reconstruction model that compresses an arbitrary number of unposed RGB views into a single fixed-size latent, and decodes an arbitrary number of oriented surface points from that latent through flow matching in $\mathbb{R}^3 \times \mathbb{S}^2$. Per-point independence in the decoder makes the model both flexible and scalable: the same shared latent supports a coarse global preview as well as million-point dense surfaces. To compensate for the lack of explicit surface coupling between independent points, we proposed a photometric guidance scheme that injects the gradient of a differentiable rendering loss into the ODE, correlating nearby points and aligning the output with the input images. As an auxiliary contribution, we built and will release a meshed version

of DL3DV [46], including $\sim 10.5\text{K}$ scenes augmented with watertight surfaces and 10^7 oriented points each. This dataset made it possible to train Surflo at scale, and we hope it will support future scene-level surface learning. On few-view 3D reconstruction benchmarks, Surflo outperforms strong baselines on standard surface metrics while being the only feed-forward model with this combination of fixed-size latent and arbitrary-resolution decoding.

Limitations. Surflo inherits VGGT’s failure modes: when the backbone provides poor pointmaps (very few views or extreme baselines), the noisy-pointmap source distribution and VGGT patch tokenization can be unreliable, hurting the decoder’s ability to recover. Photometric guidance helps but is not free: rendering oriented Gaussians adds inference cost, though inference time remains small on a single GPU for standard resolutions. Our supervision comes from Gaussian Wrapping [20] surfaces, which are themselves imperfect on transparent and textureless structures; we believe Surflo will improve as denser and cleaner ground-truth pipelines and larger datasets become available. Finally, the current model represents geometry but not appearance; extending the decoder to also predict view-dependent radiance would be a natural next step.

6 Acknowledgments

We are grateful to Maks Ovsjanikov, Patrick Pérez, and Vincent Lepetit for insightful discussions. Parts of this work were supported by the ERC Advanced Grant “explorer” (No. 101097259) and JST ASPIRE JPMJAP2305. This work was granted access to the HPC resources of IDRIS under the allocation 2025-AD011013387R3 made by GENCI.

References

- [1] Henrik Aanæs, Rasmus Ramsbøl Jensen, George Vogiatzis, Engin Tola, and Anders Bjorholm Dahl. Large-scale data for multiple-view stereopsis. *International Journal of Computer Vision (IJCV)*, 120:153–168, 2016.
- [2] Michael S. Albergo and Eric Vanden-Eijnden. Building normalizing flows with stochastic interpolants. In *International Conference on Learning Representations (ICLR)*, 2023.
- [3] Michael S. Albergo, Nicholas M. Boffi, and Eric Vanden-Eijnden. Stochastic interpolants: A unifying framework for flows and diffusions. *Journal of Machine Learning Research (JMLR)*, 2025. arXiv:2303.08797.
- [4] Arthur Allshire, Hongsuk Choi, Junyi Zhang, David McAllister, Anthony Zhang, Chung Min Kim, Trevor Darrell, Pieter Abbeel, Jitendra Malik, and Angjoo Kanazawa. Visual imitation enables contextual humanoid control. In *Proceedings of the Conference on Robot Learning (CoRL)*, 2025.
- [5] Arpit Bansal, Hong-Min Chu, Avi Schwarzschild, Soumyadip Sengupta, Micah Goldblum, Jonas Geiping, and Tom Goldstein. Universal guidance for diffusion models. In *Proceedings of the IEEE/CVF Conference on Computer Vision and Pattern Recognition Workshops (CVPRW)*, pages 843–852, 2023.
- [6] Jonathan T. Barron, Ben Mildenhall, Dor Verbin, Pratul P. Srinivasan, and Peter Hedman. Mip-NeRF 360: Unbounded anti-aliased neural radiance fields. In *Proceedings of the IEEE/CVF Conference on Computer Vision and Pattern Recognition (CVPR)*, 2022.
- [7] Jonathan T. Barron, Ben Mildenhall, Dor Verbin, Pratul P. Srinivasan, and Peter Hedman. Zip-NeRF: Anti-aliased grid-based neural radiance fields. In *Proceedings of the IEEE/CVF International Conference on Computer Vision (ICCV)*, 2023.
- [8] Eric R. Chan, Koki Nagano, Matthew A. Chan, Alexander W. Bergman, Jeong Joon Park, Axel Levy, Miika Aittala, Shalini De Mello, Tero Karras, and Gordon Wetzstein. Generative novel view synthesis with 3D-aware diffusion models. In *Proceedings of the IEEE/CVF International Conference on Computer Vision (ICCV)*, pages 4217–4229, 2023.
- [9] Jiahao Chang, Chongjie Ye, Yushuang Wu, Yuantao Chen, Yidan Zhang, Zhongjin Luo, Chenghong Li, Yihao Zhi, and Xiaoguang Han. ReconViaGen: Towards accurate multi-view 3D

- object reconstruction via generation. In *International Conference on Learning Representations (ICLR)*, 2026. arXiv:2510.23306.
- [10] David Charatan, Sizhe Lester Li, Andrea Tagliasacchi, and Vincent Sitzmann. pixelSplat: 3D Gaussian splats from image pairs for scalable generalizable 3D reconstruction. In *Proceedings of the IEEE/CVF Conference on Computer Vision and Pattern Recognition (CVPR)*, pages 19457–19467, 2024. Best Paper Runner-Up.
- [11] Weirong Chen, Chuanxia Zheng, Ganlin Zhang, Andrea Vedaldi, and Daniel Cremers. NOVA3R: Non-pixel-aligned visual transformer for amodal 3D reconstruction. In *International Conference on Learning Representations (ICLR)*, 2026. arXiv:2603.04179.
- [12] Xingyu Chen, Fu-Jen Chu, Pierre Gleize, Kevin J Liang, Alexander Sax, Hao Tang, Weiyao Wang, Michelle Guo, Thibaut Hardin, Xiang Li, et al. Sam 3d: 3dfy anything in images. *arXiv preprint arXiv:2511.16624*, 2025.
- [13] Yuedong Chen, Haofei Xu, Chuanxia Zheng, Bohan Zhuang, Marc Pollefeys, Andreas Geiger, Tat-Jen Cham, and Jianfei Cai. MVSplat: Efficient 3D Gaussian splatting from sparse multi-view images. In *European Conference on Computer Vision (ECCV)*, 2024.
- [14] Hyungjin Chung, Jeongsol Kim, Michael T. McCann, Marc L. Klasky, and Jong Chul Ye. Diffusion posterior sampling for general noisy inverse problems. In *International Conference on Learning Representations (ICLR)*, 2023.
- [15] Brian Curless and Marc Levoy. A volumetric method for building complex models from range images. In *ACM SIGGRAPH Conference Proceedings*, 1996.
- [16] Prafulla Dhariwal and Alex Nichol. Diffusion models beat GANs on image synthesis. In *Advances in Neural Information Processing Systems (NeurIPS)*, 2021.
- [17] Nicolas Dufour, Victor Besnier, Vicky Kalogeiton, and David Picard. Don’t drop your samples! coherence-aware training benefits conditional diffusion. In *Proceedings of the IEEE/CVF Conference on Computer Vision and Pattern Recognition (CVPR)*, pages 6264–6273, 2024.
- [18] Nicolas Dufour, Lucas Degeorge, Arijit Ghosh, Vicky Kalogeiton, and David Picard. MIRO: Multi-reward conditioned pretraining improves t2i quality and efficiency. *arXiv preprint arXiv:2510.25897*, 2025.
- [19] Ruiqi Gao, Aleksander Holynski, Philipp Henzler, Arthur Brussee, Ricardo Martin-Brualla, Pratul P. Srinivasan, Jonathan T. Barron, and Ben Poole. CAT3D: Create anything in 3D with multi-view diffusion models. In *Advances in Neural Information Processing Systems (NeurIPS)*, 2024.
- [20] Diego Gomez, Nissim Maruani, Antoine Guédon, Maks Ovsjanikov, and George Drettakis. From blobs to spokes: High-fidelity surface reconstruction via oriented Gaussians. *arXiv preprint arXiv:2604.07337*, 2026.
- [21] Shrisudhan Govindarajan, Daniel Rebain, Kwang Moo Yi, and Andrea Tagliasacchi. Radiant foam: Real-time differentiable ray tracing. In *Proceedings of the IEEE/CVF International Conference on Computer Vision (ICCV)*, pages 4135–4145, 2025.
- [22] Antoine Guédon and Vincent Lepetit. SuGaR: Surface-aligned Gaussian splatting for efficient 3D mesh reconstruction and high-quality mesh rendering. In *Proceedings of the IEEE/CVF Conference on Computer Vision and Pattern Recognition (CVPR)*, pages 5354–5363, 2024.
- [23] Antoine Guédon, Diego Gomez, Nissim Maruani, Bingchen Gong, George Drettakis, and Maks Ovsjanikov. MILO: Mesh-in-the-loop Gaussian splatting for detailed and efficient surface reconstruction. *ACM Transactions on Graphics (Proc. SIGGRAPH Asia)*, 44(6), 2025.
- [24] Antoine Guédon, Tomoki Ichikawa, Kohei Yamashita, and Ko Nishino. MAtCha Gaussians: Atlas of Charts for High-Quality Geometry and Photorealism From Sparse Views. In *Proceedings of the IEEE/CVF Conference on Computer Vision and Pattern Recognition (CVPR)*, 2025.

- [25] Moayed Haji-Ali, Willi Menapace, Ivan Skorokhodov, Dogyun Park, Anil Kag, Michael Vasilkovsky, Sergey Tulyakov, Vicente Ordonez, and Aliaksandr Siarohin. One model, many budgets: Elastic latent interfaces for diffusion transformers. *arXiv preprint arXiv:2603.12245*, 2026.
- [26] Yutong He, Naoki Murata, Chieh-Hsin Lai, Yuhta Takida, Toshimitsu Uesaka, Dongjun Kim, Wei-Hsiang Liao, Yuki Mitsufuji, J. Zico Kolter, Ruslan Salakhutdinov, and Stefano Ermon. Manifold Preserving Guided Diffusion. In *International Conference on Learning Representations (ICLR)*, 2024.
- [27] Peter Hedman, Julien Philip, True Price, Jan-Michael Frahm, George Drettakis, and Gabriel J. Brostow. Deep blending for free-viewpoint image-based rendering. *ACM Transactions on Graphics (Proc. SIGGRAPH Asia)*, 37(6), 2018.
- [28] Jonathan Ho and Tim Salimans. Classifier-free diffusion guidance. In *NeurIPS Workshop on Deep Generative Models and Downstream Applications*, 2021.
- [29] Jonathan Ho, Ajay Jain, and Pieter Abbeel. Denoising diffusion probabilistic models. In *Advances in Neural Information Processing Systems (NeurIPS)*, 2020.
- [30] Yicong Hong, Kai Zhang, Jiuxiang Gu, Sai Bi, Yang Zhou, Difan Liu, Feng Liu, Kalyan Sunkavalli, Trung Bui, and Hao Tan. LRM: Large reconstruction model for single image to 3D. In *International Conference on Learning Representations (ICLR)*, 2024.
- [31] Binbin Huang, Zehao Yu, Anpei Chen, Andreas Geiger, and Shenghua Gao. 2D Gaussian splatting for geometrically accurate radiance fields. In *ACM SIGGRAPH Conference Proceedings*, 2024.
- [32] Allan Jabri, David Fleet, and Ting Chen. Scalable adaptive computation for iterative generation. *arXiv preprint arXiv:2212.11972*, 2022.
- [33] Andrew Jaegle, Felix Gimeno, Andrew Brock, Andrew Zisserman, Oriol Vinyals, and João Carreira. Perceiver: General perception with iterative attention. In *International Conference on Machine Learning (ICML)*, 2021.
- [34] Andrew Jaegle, Sébastien Borgeaud, Jean-Baptiste Alayrac, Carl Doersch, Catalin Ionescu, David Ding, Skanda Koppula, Daniel Zoran, Andrew Brock, Evan Shelhamer, et al. Perceiver IO: A general architecture for structured inputs and outputs. In *International Conference on Learning Representations (ICLR)*, 2022.
- [35] Wonbong Jang, Philippe Weinzaepfel, Vincent Leroy, Lourdes Agapito, and Jérôme Revaud. Pow3R: Empowering unconstrained 3D reconstruction with camera and scene priors. In *Proceedings of the IEEE/CVF Conference on Computer Vision and Pattern Recognition (CVPR)*, pages 1071–1081, 2025.
- [36] Hyun Jun Jung, Weihang Li, Shun-Cheng Wu, William Bittner, Nikolas Brasch, Jifei Song, Eduardo Pérez-Pellitero, Zhensong Zhang, Arthur Moreau, Nassir Navab, and Benjamin Busam. SCRREAM: SCan, register, REnd and map: A framework for annotating accurate and dense 3D indoor scenes with a benchmark. In *Advances in Neural Information Processing Systems (NeurIPS) Datasets and Benchmarks Track*, 2024.
- [37] Tero Karras, Miika Aittala, Timo Aila, and Samuli Laine. Elucidating the design space of diffusion-based generative models. In *Advances in Neural Information Processing Systems (NeurIPS)*, 2022.
- [38] Michael Kazhdan, Matthew Bolitho, and Hugues Hoppe. Poisson surface reconstruction. In *Symposium on Geometry Processing (SGP)*, 2006.
- [39] Nikhil Keetha, Norman Müller, Johannes Schönberger, Lorenzo Porzi, Yuchen Zhang, Tobias Fischer, Arno Knapitsch, Duncan Zauss, Ethan Weber, Nelson Antunes, Jonathon Luiten, Manuel Lopez-Antequera, Samuel Rota Bulò, Christian Richardt, Deva Ramanan, Sebastian Scherer, and Peter Kotschieder. MapAnything: Universal feed-forward metric 3D reconstruction. In *International Conference on 3D Vision (3DV)*, 2026.

- [40] Bernhard Kerbl, Georgios Kopanas, Thomas Leimkühler, and George Drettakis. 3D Gaussian splatting for real-time radiance field rendering. *ACM Transactions on Graphics (Proc. SIGGRAPH)*, 42(4), 2023.
- [41] Felix Klein. Vergleichende Betrachtungen über neuere geometrische Forschungen. *Mathematische Annalen*, 43:63–100, 1893.
- [42] Arno Knapitsch, Jaesik Park, Qian-Yi Zhou, and Vladlen Koltun. Tanks and temples: Benchmarking large-scale scene reconstruction. *ACM Transactions on Graphics (Proc. SIGGRAPH)*, 36(4), 2017.
- [43] Vincent Leroy, Yohann Cabon, and Jérôme Revaud. Grounding image matching in 3D with MAST3R. In *European Conference on Computer Vision (ECCV)*, 2024.
- [44] Tianhong Li, Yonglong Tian, He Li, Mingyang Deng, and Kaiming He. Autoregressive image generation without vector quantization. In *Advances in Neural Information Processing Systems (NeurIPS)*, 2024.
- [45] Haotong Lin, Sili Chen, Jun Hao Liew, Donny Y. Chen, Zhenyu Li, Guang Shi, Jiashi Feng, and Bingyi Kang. Depth anything 3: Recovering the visual space from any views. *arXiv preprint arXiv:2511.10647*, 2025.
- [46] Lu Ling, Yichen Sheng, Zhi Tu, Wentian Zhao, Cheng Xin, Kun Wan, Lantao Yu, Qianyu Guo, Zixun Yu, Yawen Lu, Xuanmao Li, Xingpeng Sun, Rohan Ashok, Aniruddha Mukherjee, Hao Kang, Xiangrui Kong, Gang Hua, Tianyi Zhang, Bedrich Benes, and Aniket Bera. DL3DV-10K: A large-scale scene dataset for deep learning-based 3D vision. In *Proceedings of the IEEE/CVF Conference on Computer Vision and Pattern Recognition (CVPR)*, pages 22160–22169, 2024.
- [47] Yaron Lipman, Ricky T. Q. Chen, Heli Ben-Hamu, Maximilian Nickel, and Matt Le. Flow matching for generative modeling. In *International Conference on Learning Representations (ICLR)*, 2023.
- [48] Minghua Liu, Chao Xu, Haian Jin, Linghao Chen, T. Mukund Varma, Zexiang Xu, and Hao Su. One-2-3-45: Any single image to 3D mesh in 45 seconds without per-shape optimization. In *Advances in Neural Information Processing Systems (NeurIPS)*, 2023.
- [49] Ruoshi Liu, Rundi Wu, Basile Van Hoorick, Pavel Tokmakov, Sergey Zakharov, and Carl Vondrick. Zero-1-to-3: Zero-shot one image to 3D object. In *Proceedings of the IEEE/CVF International Conference on Computer Vision (ICCV)*, 2023.
- [50] Xingchao Liu, Chengyue Gong, and Qiang Liu. Flow straight and fast: Learning to generate and transfer data with rectified flow. In *International Conference on Learning Representations (ICLR)*, 2023.
- [51] Xiaoxiao Long, Yuan-Chen Guo, Cheng Lin, Yuan Liu, Zhiyang Dou, Lingjie Liu, Yuexin Ma, Song-Hai Zhang, Marc Habermann, Christian Theobalt, and Wenping Wang. Wonder3D: Single image to 3D using cross-domain diffusion. In *Proceedings of the IEEE/CVF Conference on Computer Vision and Pattern Recognition (CVPR)*, 2024.
- [52] William E. Lorensen and Harvey E. Cline. Marching cubes: A high resolution 3D surface construction algorithm. In *ACM SIGGRAPH Computer Graphics*, volume 21, pages 163–169, 1987.
- [53] Ben Mildenhall, Pratul P. Srinivasan, Matthew Tancik, Jonathan T. Barron, Ravi Ramamoorthi, and Ren Ng. NeRF: Representing scenes as neural radiance fields for view synthesis. In *European Conference on Computer Vision (ECCV)*, 2020.
- [54] Thomas Müller, Alex Evans, Christoph Schied, and Alexander Keller. Instant neural graphics primitives with a multiresolution hash encoding. *ACM Transactions on Graphics (Proc. SIGGRAPH)*, 41(4), 2022.
- [55] Alex Nichol, Heewoo Jun, Pratul Dhariwal, Pamela Mishkin, and Mark Chen. Point-E: A system for generating 3D point clouds from complex prompts. *arXiv preprint arXiv:2212.08751*, 2022.

- [56] William Peebles and Saining Xie. Scalable diffusion models with transformers. In *Proceedings of the IEEE/CVF International Conference on Computer Vision (ICCV)*, pages 4195–4205, 2023.
- [57] Ben Poole, Ajay Jain, Jonathan T. Barron, and Ben Mildenhall. DreamFusion: Text-to-3D using 2D diffusion. In *International Conference on Learning Representations (ICLR)*, 2023.
- [58] Mike Roberts, Jason Ramapuram, Anurag Ranjan, Atulit Kumar, Miguel Angel Bautista, Nathan Paczan, Russ Webb, and Joshua M. Susskind. Hypersim: A photorealistic synthetic dataset for holistic indoor scene understanding. In *Proceedings of the IEEE/CVF International Conference on Computer Vision (ICCV)*, 2021.
- [59] Robin Rombach, Andreas Blattmann, Dominik Lorenz, Patrick Esser, and Björn Ommer. High-resolution image synthesis with latent diffusion models. In *Proceedings of the IEEE/CVF Conference on Computer Vision and Pattern Recognition (CVPR)*, pages 10684–10695, 2022.
- [60] Jiaming Song, Chenlin Meng, and Stefano Ermon. Denoising diffusion implicit models. In *International Conference on Learning Representations (ICLR)*, 2021.
- [61] Jiaming Song, Qinsheng Zhang, Hongxu Yin, Morteza Mardani, Ming-Yu Liu, Jan Kautz, Yongxin Chen, and Arash Vahdat. Loss-guided diffusion models for plug-and-play controllable generation. In *International Conference on Machine Learning (ICML)*, 2023.
- [62] Yang Song, Jascha Sohl-Dickstein, Diederik P. Kingma, Abhishek Kumar, Stefano Ermon, and Ben Poole. Score-based generative modeling through stochastic differential equations. In *International Conference on Learning Representations (ICLR)*, 2021.
- [63] Stanislaw Szymanowicz, Christian Rupprecht, and Andrea Vedaldi. Splatter image: Ultra-fast single-view 3D reconstruction. In *Proceedings of the IEEE/CVF Conference on Computer Vision and Pattern Recognition (CVPR)*, pages 10208–10217, 2024.
- [64] Matthew Tancik, Pratul P. Srinivasan, Ben Mildenhall, Sara Fridovich-Keil, Nithin Raghavan, Utkarsh Singhal, Ravi Ramamoorthi, Jonathan T. Barron, and Ren Ng. Fourier features let networks learn high frequency functions in low dimensional domains. In *Advances in Neural Information Processing Systems (NeurIPS)*, 2020.
- [65] Shinji Umeyama. Least-Squares Estimation of Transformation Parameters Between Two Point Patterns. *IEEE Transactions on Pattern Analysis and Machine Intelligence*, 13(4):376–380, 1991.
- [66] Arash Vahdat, Francis Williams, Zan Gojcic, Or Litany, Sanja Fidler, and Karsten Kreis. LION: Latent point diffusion models for 3D shape generation. In *Advances in Neural Information Processing Systems (NeurIPS)*, 2022.
- [67] Hengyi Wang and Lourdes Agapito. 3D reconstruction with spatial memory. In *International Conference on 3D Vision (3DV)*, 2025. arXiv:2408.16061, 2024.
- [68] Jianyuan Wang, Minghao Chen, Nikita Karaev, Andrea Vedaldi, Christian Rupprecht, and David Novotny. VGGT: Visual geometry grounded transformer. In *Proceedings of the IEEE/CVF Conference on Computer Vision and Pattern Recognition (CVPR)*, pages 5294–5306, 2025. Best Paper Award.
- [69] Peng Wang, Lingjie Liu, Yuan Liu, Christian Theobalt, Taku Komura, and Wenping Wang. NeuS: Learning neural implicit surfaces by volume rendering for multi-view reconstruction. In *Advances in Neural Information Processing Systems (NeurIPS)*, 2021.
- [70] Qianqian Wang, Yifei Zhang, Aleksander Holynski, Alexei A. Efros, and Angjoo Kanazawa. Continuous 3D perception model with persistent state. In *Proceedings of the IEEE/CVF Conference on Computer Vision and Pattern Recognition (CVPR)*, pages 10510–10522, 2025.
- [71] Ruicheng Wang, Sicheng Xu, Cassie Dai, Jianfeng Xiang, Yu Deng, Xin Tong, and Jiaolong Yang. MoGe: Unlocking accurate monocular geometry estimation for open-domain images with optimal training supervision. In *Proceedings of the IEEE/CVF Conference on Computer Vision and Pattern Recognition (CVPR)*, pages 5261–5271, 2025.

- [72] Ruicheng Wang, Sicheng Xu, Yue Dong, Yu Deng, Jianfeng Xiang, Zelong Lv, Guangzhong Sun, Xin Tong, and Jiaolong Yang. MoGe-2: Accurate monocular geometry with metric scale and sharp details. In *Advances in Neural Information Processing Systems (NeurIPS)*, 2025.
- [73] Shuzhe Wang, Vincent Leroy, Yohann Cabon, Boris Chidlovskii, and Jérôme Revaud. DUS_t3R: Geometric 3D vision made easy. In *Proceedings of the IEEE/CVF Conference on Computer Vision and Pattern Recognition (CVPR)*, 2024.
- [74] Yifan Wang, Jianjun Zhou, Haoyi Zhu, Wenzheng Chang, Yang Zhou, Zizun Li, Junyi Chen, Jiangmiao Pang, Chunhua Shen, and Tong He. π^3 : Permutation-equivariant visual geometry learning. In *International Conference on Learning Representations (ICLR)*, 2026. arXiv:2507.13347.
- [75] Zhengyi Wang, Cheng Lu, Yikai Wang, Fan Bao, Chongxuan Li, Hang Su, and Jun Zhu. ProlificDreamer: High-fidelity and diverse text-to-3D generation with variational score distillation. In *Advances in Neural Information Processing Systems (NeurIPS)*, 2023.
- [76] Frederik Warburg, Ethan Weber, Matthew Tancik, Aleksander Holynski, and Angjoo Kanazawa. NeRFbusters: Removing ghostly artifacts from casually captured NeRFs. In *Proceedings of the IEEE/CVF International Conference on Computer Vision (ICCV)*, 2023.
- [77] Dongxu Wei, Qi Xu, Zhiqi Li, Hangning Zhou, Cong Qiu, Hailong Qin, Mu Yang, Zhaopeng Cui, and Peidong Liu. Any 3D scene is worth 1K tokens: 3D-grounded representation for scene generation at scale. *arXiv preprint arXiv:2604.11331*, 2025. Project: <https://wswdx.github.io/3DRAE/>.
- [78] Rundi Wu, Ben Mildenhall, Philipp Henzler, Keunhong Park, Ruiqi Gao, Daniel Watson, Pratul P. Srinivasan, Dor Verbin, Jonathan T. Barron, Ben Poole, and Aleksander Holynski. ReconFusion: 3D reconstruction with diffusion priors. In *Proceedings of the IEEE/CVF Conference on Computer Vision and Pattern Recognition (CVPR)*, pages 21551–21561, 2024.
- [79] Ziyuan Xia, Jingyi Xu, Chong Cui, Yuanhong Yu, Jiazhao Zhang, Qingsong Yan, Tao Ni, Junbo Chen, Xiaowei Zhou, Hujun Bao, Ruizhen Hu, and Sida Peng. Habitat-gs: A high-fidelity navigation simulator with dynamic gaussian splatting. *arXiv preprint arXiv:2604.12626*, 2026.
- [80] Jianfeng Xiang, Zelong Lv, Sicheng Xu, Yu Deng, Ruicheng Wang, Bowen Zhang, Dong Chen, Xin Tong, and Jiaolong Yang. Structured 3D latents for scalable and versatile 3D generation. In *Proceedings of the IEEE/CVF Conference on Computer Vision and Pattern Recognition (CVPR)*, 2025. Spotlight; arXiv:2412.01506, 2024.
- [81] Jiale Xu, Weihao Cheng, Yiming Gao, Xintao Wang, Shenghua Gao, and Ying Shan. InstantMesh: Efficient 3D mesh generation from a single image with sparse-view large reconstruction models. *arXiv preprint arXiv:2404.07191*, 2024.
- [82] Guandao Yang, Xun Huang, Zekun Hao, Ming-Yu Liu, Serge Belongie, and Bharath Hariharan. PointFlow: 3D point cloud generation with continuous normalizing flows. In *Proceedings of the IEEE/CVF International Conference on Computer Vision (ICCV)*, 2019.
- [83] Jianing Yang, Alexander Sax, Kevin J. Liang, Mikael Henaff, Hao Tang, Ang Cao, Joyce Chai, Franziska Meier, and Matt Feiszli. Fast3R: Towards 3D reconstruction of 1000+ images in one forward pass. In *Proceedings of the IEEE/CVF Conference on Computer Vision and Pattern Recognition (CVPR)*, pages 21924–21935, 2025.
- [84] Yao Yao, Zixin Luo, Shiwei Li, Jingyang Zhang, Yufan Ren, Lei Zhou, Tian Fang, and Long Quan. BlendedMVS: A large-scale dataset for generalized multi-view stereo networks. In *Proceedings of the IEEE/CVF Conference on Computer Vision and Pattern Recognition (CVPR)*, 2020.
- [85] Lior Yariv, Jiatao Gu, Yoni Kasten, and Yaron Lipman. Volume rendering of neural implicit surfaces. In *Advances in Neural Information Processing Systems (NeurIPS)*, 2021.
- [86] Botao Ye, Sifei Liu, Haofei Xu, Xueting Li, Marc Pollefeys, Ming-Hsuan Yang, and Songyou Peng. No pose, no problem: Surprisingly simple 3D Gaussian splats from sparse unposed images. In *International Conference on Learning Representations (ICLR)*, 2025. arXiv:2410.24207.

- [87] Zehao Yu, Torsten Sattler, and Andreas Geiger. Gaussian opacity fields: Efficient adaptive surface reconstruction in unbounded scenes. *ACM Transactions on Graphics (Proc. SIGGRAPH Asia)*, 2024.
- [88] Baowen Zhang, Chuan Fang, Rakesh Shrestha, Yixun Liang, Xiaoxiao Long, and Ping Tan. RaDe-GS: Rasterizing depth in Gaussian splatting. *ACM Transactions on Graphics*, 2026. arXiv:2406.01467.
- [89] Biao Zhang, Jiapeng Tang, Matthias Nießner, and Peter Wonka. 3DShape2VecSet: A 3D shape representation for neural fields and generative diffusion models. *ACM Transactions on Graphics (Proc. SIGGRAPH)*, 42(4), 2023.
- [90] Biao Zhang, Jing Ren, and Peter Wonka. Geometry distributions. In *Proceedings of the IEEE/CVF International Conference on Computer Vision (ICCV)*, 2025.
- [91] Chuhan Zhang, Guillaume Le Moing, Skanda Koppula, Ignacio Rocco, Liliane Momeni, Junyu Xie, Shuyang Sun, Rahul Sukthankar, Joëlle K. Barral, Raia Hadsell, Zoubin Ghahramani, Andrew Zisserman, Junlin Zhang, and Mehdi S. M. Sajjadi. Efficiently Reconstructing Dynamic Scenes One D4RT at a Time. In *Proceedings of the IEEE/CVF Conference on Computer Vision and Pattern Recognition (CVPR)*, 2026.
- [92] Kai Zhang, Sai Bi, Hao Tan, Yuanbo Xiangli, Nanxuan Zhao, Kalyan Sunkavalli, and Zexiang Xu. GS-LRM: Large reconstruction model for 3D Gaussian splatting. In *European Conference on Computer Vision (ECCV)*, 2024.
- [93] Longwen Zhang, Ziyu Wang, Qixuan Zhang, Qiwei Qiu, Anqi Pang, Haoran Jiang, Wei Yang, Lan Xu, and Jingyi Yu. CLAY: A controllable large-scale generative model for creating high-quality 3D assets. *ACM Transactions on Graphics (Proc. SIGGRAPH)*, 43(4), 2024.
- [94] Zibo Zhao, Wen Liu, Xin Chen, Xianfang Zeng, Rui Wang, Pei Cheng, Bin Fu, Tao Chen, Gang Yu, and Shenghua Gao. Michelangelo: Conditional 3D shape generation based on shape-image-text aligned latent representation. In *Advances in Neural Information Processing Systems (NeurIPS)*, 2023.
- [95] Zibo Zhao, Zeqiang Lai, Qingxiang Lin, Yunfei Zhao, Haolin Liu, Shuhui Yang, Yifei Feng, Mingxin Yang, Sheng Zhang, Xianghui Yang, et al. Hunyuan3D 2.0: Scaling diffusion models for high resolution textured 3D assets generation. *arXiv preprint arXiv:2501.12202*, 2025.
- [96] Chen Ziwen, Hao Tan, Kai Zhang, Sai Bi, Fujun Luan, Yicong Hong, Li Fuxin, and Zexiang Xu. Long-LRM: Long-sequence large reconstruction model for wide-coverage Gaussian splats. In *Proceedings of the IEEE/CVF International Conference on Computer Vision (ICCV)*, pages 4349–4359, 2025.

A Related work

Per-view feed-forward 3D geometry. The first family of feed-forward 3D models predicts a pointmap or depth map per input image. DUST3R [73] pioneered this paradigm by regressing paired pointmaps in a common frame from two views, and Leroy et al. [43] extended it to more accurate matching. More recent work scales the idea to many views with a single transformer: VGGT [68] processes hundreds of images in one forward pass, Lin et al. [45] pushes the formulation further with a depth-ray prediction target, Yang et al. [83] parallelises DUST3R-style decoding across 1000+ views, and Wang et al. [74] removes the dependency on a fixed reference frame. Streaming variants such as Spann3R [67] and ingredients such as metric monocular pointmaps [71, 72], prior-conditioned regression [35], and unified factored representations [39] further enrich this space. These models are remarkably accurate per view, but the output remains *view-bound*: the number of predicted tokens grows linearly with the number of inputs, the per-view pointmaps overlap heavily, and they are rarely consistent enough to be fused into a clean mesh [4].

Latent and global feed-forward 3D. A second line of work attempts to keep a single, view-agnostic representation. CUT3R [70] maintains a persistent state through cross-attention but still reads it out with per-view metric pointmaps. Concurrent global tokenization approaches such as 3DRAE [77] target this goal but, in practice, still query the latent through per-view decodings. Recent work NOVA3R [11] is the closest to our setting: it compresses unposed multi-view inputs into a fixed-size latent and decodes points with a flow-matching head, but emits a fixed number of 3D points with no ability to sample more or less. Furthermore, it is trained with at most 2 input views, limiting its ability to fully reconstruct the entire scene. Closely related in spirit, D4RT [91] also encodes the input into a single global scene representation that is decoded by independent point queries. It is, however, designed for *dense video*: its encoder operates on a temporally-patchified frame sequence to target 4D reconstruction, and it decodes by regressing the 3D position of *pixel-anchored* spatio-temporal queries rather than generatively transporting free oriented points onto a surface. Surflo instead targets sparse images and decodes arbitrary 3D points through flow matching. Generalisable Gaussian-splatting models follow a related philosophy: pixelSplat, MVSplat, NoPoSplat [10, 13, 86] and the LRM family [30, 92, 96, 63] predict per-pixel or per-view 3D Gaussians from a few sparse images, sharing the redundancy issue of pointmap methods. On the architectural side, our encoder is a Perceiver [33, 34], an architecture that has been repurposed as a generative backbone in recurrent interface networks (RIN) [32, 17, 18, 25] for image generation; we adapt it here to feed-forward 3D by compressing multi-view tokens into a fixed-size latent that is then exposed through a decoder that can sample arbitrary number of oriented points directly in the 3D space. Surflo differs from this entire family in that it produces a single, fixed-size, view-independent latent *and* exposes the geometry through an arbitrary-resolution decoder.

Per-scene optimization for surfaces. At the scene scale, fine-grained 3D reconstruction is still dominated by per-scene optimization. One branch targets photo-realistic novel-view synthesis without explicit surfaces: NeRF [53] and its accelerated or anti-aliased successors [54, 6, 7], 3D Gaussian Splatting [40], and recent variants such as Radiant Foam [21], all of which fit a radiance field that produces faithful renderings but no clean geometry. The other branch is explicitly geometry-focused: NeuS [69] and VolSDF [85] render an implicit signed-distance field, while SuGaR [22], 2D Gaussian Splatting [31], Gaussian Opacity Fields [87], RaDe-GS [88], MILo [23] and Gaussian Wrapping [20] build on radiance-field representations to extract a manifold-quality mesh, often combined with classical surface-extraction machinery [52, 15, 38]. Both branches reach high fidelity but share the same practical limits: they rely on dense captures of hundreds of images, require tens of minutes of per-scene optimization, and yield no reusable latent. Sparse-view variants such as Guédon et al. [24] relax the input requirement, yet their time and memory cost scales linearly with the number of views, limiting their scalability. Surflo instead leverages Gaussian Wrapping [20] only at training time, as a source of dense surface supervision, and is itself feed-forward and scene-level at inference: it decodes surfaces at arbitrary resolution from a single shared latent from unposed input images, decoupling the cost of reconstruction from the number of input views.

Object-level learned 3D and shape latents. Feed-forward learned mesh predictors offer an alternative to optimization, but remain largely *object-level*: LRM and its Gaussian-splatting variant GS-LRM [30, 92] regress NeRFs or 3DGS from one or a few posed views, InstantMesh [81] adds an iso-surface extraction head, and TRELIS [80] learns a structured latent for object generation with a

rectified-flow transformer. Sam3D [12] predicts 3D geometry and texture from a single image. Closer to our own design, 3DShape2VecSet [89], Michelangelo [94] and CLAY [93] represent shapes as a small set of latent vectors decoded by cross-attention, and a wide ecosystem of 3D-native generators built on this idea reconstructs single objects from images or text [49, 48, 51, 95]. None of these methods targets full scenes from a few unposed views with a shared, queryable latent, which is precisely Surflo’s regime.

Diffusion / flow priors and guidance. A growing line of work uses 2D diffusion as a prior for novel-view synthesis or 3D reconstruction: GeNVS [8], CAT3D [19] and ReconFusion [78] hallucinate plausible views that are then turned into geometry through an external pipeline, NeRFbusters [76] works directly in 3D as a voxel-based regulariser, and ReconViaGen [9] distils generative priors into object reconstruction. Score-distillation methods [57, 75] push the same idea further at the price of long per-scene optimization. Their target is pixels or single objects rather than a global, queryable scene representation. The closest mathematical tool to ours is flow matching and its relatives [47, 50, 2, 3], which build on diffusion foundations [29, 60, 62, 37, 59, 56] and were already shown to be effective for point clouds and meshes in PointFlow, LION, Point-E, Geometry Distributions, and TRELLIS [82, 66, 55, 90, 80]. Instead of denoising images, our decoder learns a velocity field that transports query points in \mathbb{R}^3 *independently* from a noisy source to the surface, conditioned on the scene latent. Conceptually, this design echoes MAR [44] in image generation: MAR pairs a global autoregressive prior over image tokens with a per-token diffusion head, sampling each patch conditioned on a global state; Surflo analogously pairs a global feed-forward prior, built on VGGT [68], with a per-point flow-matching head, replacing patch-wise transport in pixel space with point-wise transport in \mathbb{R}^3 . The guidance mechanism we use during ODE integration is reminiscent of classifier and classifier-free guidance [16, 28] and of training-free inverse-problem solvers [14, 5, 61], but here the gradient signal comes from a differentiable photometric rendering of the partially solved point cloud rather than from an external classifier or likelihood.

B Architecture details

We give in this section the exact hyperparameters of the encoder and decoder used in all main experiments.

Encoder. The frozen VGGT-1B [68] backbone (24 transformer blocks, patch size 14, input resolution 518×280) produces $37 \times 20 = 740$ patch tokens per view per layer and 1 camera token per view, all of dimension $d_v = 2048$. We extract tokens from layers $\ell \in \{4, 11, 17, 23\}$. We then project to a working dimension $D = 512$ with a single linear layer; a separate linear layer projects the camera tokens. The 3D Gaussian Fourier features [64] use $F = 512$ frequencies sampled from $\mathcal{N}(0, \sigma^2 \mathbf{I}_3)$ distributed over 16 log-spaced bands with $\sigma \in \{100, 64.94, \dots, 0.237, 0.154\}$ (geometric ratio ≈ 0.65), 32 frequencies per band, expressed in scene-normalized coordinates (coordinates are normalized by the median distance to the median VGGT point). The same encoder configuration is shared with the query-point spatial encoder of the decoder, and the resulting 3D PE is broadcast across the four intermediate VGGT layers. The Perceiver encoder uses $K = 128$ learnable latent tokens and $L_s = 4$ self-attention blocks with 16 heads after each of the $L_e = 4$ cross-attention with patch tokens, with `mlp_ratio = 4.0`, `qk-norm`, `LayerScale` initialized at 0.01. The Perceiver encoder for camera tokens applies cross-attention of 1 latent token with camera tokens for 4 times, with 16 heads and no self-attention. The patch and camera latents are kept on separate paths and consumed by the decoder through different mechanisms (cross-attention for the patch latents, AdaLN conditioning for the camera latent).

Decoder. The flow-matching decoder is a $L = 12$ -layer transformer with hidden dimension $D = 512$ and 16 heads, `mlp_ratio = 4.0`, and `qk-norm`. There is no self-attention over query points: each block processes points independently, and all spatial information sharing is delegated to the encoder latents. Each of the first 6 blocks alternates cross-attention to the latent \mathbf{z} and an MLP, each of which is prepended with Ada-LN with conditioning tokens (time and camera token). The latter 6 blocks apply only Ada-LN and MLP. Each AdaLN conditioning network produces shift, scale and gate parameters in the DiT [56] style $\text{LN}(x) \cdot (1 + \text{scale}) + \text{shift}$, residual gated by gate), with the projection layer zero-initialized so that every block starts as the identity. All AdaLN modules are fed with $\tau(t) + \text{MLP}_{\text{cam}}(\mathbf{z}_{\text{cam}})$, where \mathbf{z}_{cam} is the encoded camera latent and MLP_{cam} is a 2-layer

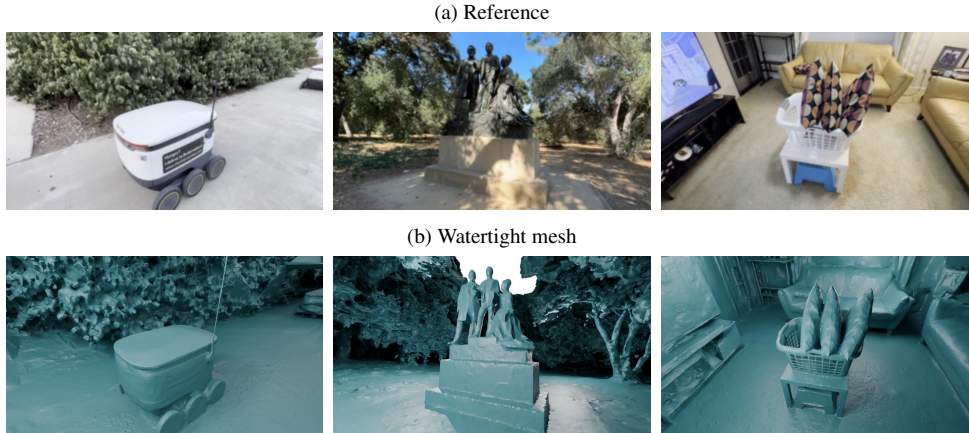


Figure 7: **Meshed DL3DV dataset.** We enrich every scene of DL3DV [46] (a) with a watertight mesh (b) and an associated oriented point cloud. For each scene we run Gaussian Wrapping [20] to extract a watertight surface, and finally sample 10^7 points uniformly on this surface together with their normals.

2048-dimensional MLP. The time embedding $\tau(t)$ uses the standard sinusoidal schedule with 512 frequencies log-spaced in $[0.1, 1000]$ (output dimension 1024, projected to $D = 512$). Query-point coordinates are normalized per-scene with the same statistics as the patch 3D PE and encoded with the 16-band Gaussian RFF encoder described above before entering the first block. A small two-layer MLP head on top of the last block predicts the per-point normal in \mathbb{S}^2 alongside the velocity, yielding a 6-dimensional output; the final LayerNorm and head are executed in FP32 for precision. Following VGGT [68], we use GeLU as the activation function, except for Ada-LN and MLP for the camera token or Fourier-encoded token projections, where we use SiLU.

Query Formulation. For numerical stability, normals are represented as a *residual* within a query point \mathbf{x} . That is, given the sampled 3D point $\mathbf{m} \in \mathbb{R}^3$ and a normal $\mathbf{n} \in \mathbb{S}^2$, the query point is initialized as $\mathbf{x}_0 = (\mathbf{m}, \mathbf{m} + \epsilon \mathbf{n}) \in \mathbb{R}^6$, where $\epsilon = 10^{-3}$ multiplied by the scene scale. Velocities are predicted in the same space. For decoding the normal from this representation at inference time, we simply take the difference between the second and the first half and normalize the resulting vector.

C Training

Meshed DL3DV dataset. We build a scene-level surface dataset by enriching every scene of DL3DV [46] with a watertight mesh and an associated oriented point cloud. For each scene we run Gaussian Wrapping [20] to extract a watertight surface, and finally sample $\sim 10^7$ points uniformly on this surface together with their normals. We will release the dataset alongside the paper as an auxiliary contribution. We cache the VGGT tokens once per scene and per view set to avoid recomputing them at every epoch. Figure 7 shows examples from the dataset.

Training. The decoder is trained as a velocity-prediction flow-matching model with the conditional optimal-transport scheduler of [47]. The starting state \mathbf{x}_0 for each query point is sampled as the VGGT world-point prediction (estimated depth values back-projected using estimated camera parameters) plus isotropic Gaussian noise of standard deviation 0.1 (in scene-normalized coordinates). Time samples are drawn from a logit-normal distribution $t = \sigma(z)$ with $z \sim \mathcal{N}(1.0, 1.6^2)$, biasing supervision towards $t \rightarrow 1$. With probability 0.1 the VGGT features are masked to zero during training to enable classifier-free guidance at inference.

Aligning GT to Predicted Points. The flow-matching objective supervises each query point against the ground-truth surface, but the two live in different coordinate frames: the ground-truth points are given in the original COLMAP frame of the dataset, whereas the predicted points follow the VGGT convention. We must therefore align them before computing the loss. This alignment has to be accurate enough to preserve fine geometric detail in the supervision, yet fast enough to run at every training step. We estimate an affine transform (\mathbf{L}, \mathbf{t}) that maps COLMAP world coordinates

into the VGGT frame, i.e. $\mathbf{p}_{\text{vggt}} \approx \mathbf{p}_{\text{colmap}}\mathbf{L} + \mathbf{t}$. The transform is fitted from depth maps of the ground-truth mesh rendered from the COLMAP cameras, which we precompute for each scene and store as part of the dataset.

We first discard unreliable points by keeping only the top 25% of pixels ranked by VGGT depth confidence, then proceed in two steps. The first step produces a coarse but robust similarity alignment from the *reference camera alone*: we take only its ground-truth depth points, express them in the reference camera’s view space through the COLMAP extrinsics, isotropically rescale them by the ratio of the VGGT and COLMAP camera-baseline extents (the mean distance of the camera centers to their centroid), and move them into the VGGT world frame using the corresponding VGGT camera pose. Because the rotation, translation, and scale are derived from camera geometry rather than from matching depth values, this step is insensitive to per-pixel depth noise and yields a reliable initialization. The second step refines this initialization into a full affine transform. For each camera, we measure the residual between the coarsely aligned ground-truth depth points and the VGGT depth points, normalize it by a characteristic spatial scale, and turn it into robust per-point weights via a soft-min; correspondences whose weight falls below the per-camera median are treated as outliers and dropped. A single weighted least-squares fit over the surviving depth points from all cameras then yields the final transform.

D Guidance

Time grid. We use a bi-phase time grid of $50 + 100$ steps with a phase switch at $t = 0.95$, sampling $P = 10^5$ query points by default. At each step $t_k \geq 0.95$ the network predicts the velocity, from which we recover an estimate $\hat{\mathbf{x}}_1$ of the clean sample (point positions and, in the \mathbb{R}^6 point-normal parameterization, per-point normals).

Rendering guidance. The key idea of *rendering guidance* is to nudge this trajectory, in its final phase, so that the implied surface is photometrically and geometrically consistent with the input images. Guidance is activated only once $t \geq \tau_g = 0.95$. At activation, the current estimate $\hat{\mathbf{x}}_1$ is used to instantiate a set of 3D Gaussians, one per generated point, whose learnable attributes are anisotropic log-scales, rotation quaternions, opacity, and view-dependent color (spherical harmonics up to degree 3).

Inner loop. At every subsequent ODE step we run an inner loop of $M = 32$ gradient descent iterations that differentially renders these Gaussians (via the RaDe-GS rasterizer [88]) into input views and minimizes a composite rendering loss [24, 20]. After the inner loop, the Gaussian displacements define a refined target $\hat{\mathbf{x}}_g$, which we convert back into a velocity; the ODE step is then taken with this *guided* velocity, so that the rendering gradients steer the generative trajectory. We additionally backpropagate the rendering gradients to the camera poses to account for potential, small pose errors in the VGGT predictions.

Monocular geometric experts. An additional, optional guidance term injects priors from an off-the-shelf monocular expert [45]. Following [24, 23], we use a scale-invariant depth-order loss between the rendered depth and the monocular depth prior. Only relative ordering is enforced, preventing the multi-view inconsistency of monocular depth predictions from affecting the flow trajectory.

Filtering outliers. The rendering guidance mechanism provides a natural criterion to detect outliers in the flow: noisy points and floaters that do not contribute to any input view converge to a low opacity. We exploit this signal to prune low-opacity points on the fly during the ODE integration, following the standard pruning threshold of 3D Gaussian Splatting [40].

E Evaluation protocol.

To ensure a fair comparison, all baselines receive the same set of unposed views for each scene, and latent methods are evaluated from their official checkpoints. Per-view, pointmap-based methods [68, 45] do not produce a single surface, so we fuse their predictions with TSDF fusion [15]. To recover both foreground and background geometry while preserving fine detail in the foreground, we use a

multi-resolution voxel grid: three nested grids of 100^3 voxels each, with side lengths of 1, 3 and 10 times the scene diagonal, and a TSDF truncation margin of 1.25% of the scene diagonal.

Point cloud alignment. To compare a predicted point cloud against the ground-truth surface, we first bring the prediction into the ground-truth coordinate frame and then measure geometric agreement. All distance thresholds are expressed as fractions of the ground-truth bounding-box diagonal $d = \|\mathbf{p}_{\max} - \mathbf{p}_{\min}\|$, so that the protocol is invariant to the absolute scale of each scene. Alignment proceeds in two stages. First, we estimate a closed-form 7-DoF similarity transform (scale, rotation, and translation) with the Umeyama algorithm [65], using the predicted and ground-truth camera centers as correspondences; this fixes the global scale. Second, we refine the rigid component with a scale-locked, robust point-to-point ICP, in which the Umeyama scale is held fixed and only rotation and translation are updated. ICP runs for up to 30 iterations on voxel-downsampled clouds (voxel size $10^{-3}d$). In each iteration, correspondences beyond a truncation distance are discarded, where the truncation radius follows a geometric schedule from $5 \times 10^{-2}d$ down to $10^{-2}d$ so that early iterations are permissive and later ones strict. Of the surviving correspondences we retain only the closest 70% (least-trimmed squares), weight their residuals with a Huber loss (with δ set to half the current truncation radius), and solve a weighted Procrustes problem for the rigid update.

Metrics. After alignment, we clip prediction points lying outside the axis-aligned ground-truth bounding box to avoid asymmetrically inflating the prediction-to-ground-truth distance term. Finally, both clouds are voxel-downsampled to a common density (voxel size $10^{-3}d$), and we report the symmetric Chamfer distance together with the F-score at a distance threshold $\tau = 10^{-2}d$. Chamfer distances are reported normalized by d to allow for aggregation across scenes of differing absolute scale.